


# Nonlinear Landau-Zener-Stückelberg-Majorana tunneling and interferometry of extended Bose-Hubbard flux ladders

Xin Qiao, Xiao-Bo Zhang, Yue Jian, Yun-E Ma, Rui Gao, Ai-Xia Zhang, and Ju-Kui Xue \*

*College of Physics and Electronics Engineering, Northwest Normal University, Lanzhou 730070, China*



(Received 6 March 2023; accepted 11 September 2023; published 21 September 2023)

The nonlinear Landau-Zener-Stückelberg-Majorana (LZSM) tunneling dynamics and interferometry of an extended Bose-Hubbard flux ladder are studied. Based on the mean-field theory, the dispersion relation of the system is given, and it is found that loop structures periodically appear in the band structure and the nonlinear LZSM interference occurs naturally without Floquet engineering, which can be effectively modulated by atomic interactions. The nonlinear energy bands and the unique chirality feature of the flux ladder system can be identified through the dynamics of nonlinear Landau-Zener tunneling. Remarkably, the critical position of the noise in the interference pattern can be employed to identify the loop structure in the energy band, establishing an effective link between the nonlinear loop structure and LZSM interferometry. The position, intensity, symmetry, and width of interference patterns strongly depend on the magnetic field, atomic interactions, rung-to-leg coupling ratio, and energy bias, which provides an effective way to measure these parameters using the nonlinear LZSM interferometry. This paper further expands the dynamics of flux ladder systems to complex interaction regions and has potential applications in the precise measurement of related nonlinear systems.

DOI: [10.1103/PhysRevE.108.034214](https://doi.org/10.1103/PhysRevE.108.034214)

## I. INTRODUCTION

For a quantum system with a time-dependent Hamiltonian, it is usually difficult to derive a complete analytical expression of the dynamics. One of the few analytically solved examples is the well-known Landau-Zener problem [1–4], which serves as an idealized model applicable to various dynamic processes in different contexts, including molecular collisions [5], nanosystems [6,7], waveguide systems [8,9], and quantum information processing [10,11]. The Landau-Zener-Stückelberg-Majorana (LZSM) interference [12–15] has also emerged as a powerful tool for precise measurements in quantum dots, quasi-one-dimensional layered materials, superconducting qubits, and Rydberg atoms [16–22]. Since some nonlinear effects are unavoidable in actual physical systems, the nonlinear Landau-Zener problem has drawn extensive attention recently [23–28]. A comprehensive analysis of the nonlinear Landau-Zener tunneling reveals that nonlinearity induces the loop structure of the energy band structure and increases the tunneling rate in the adiabatic limit [24,25,29,30]. Further investigations for nonlinear LZSM interference have demonstrated that the symmetry, position, width, and intensity of interference fringes strongly depend on the nonlinear interaction [31]. The non-Hermitian effects of the Landau-Zener transition and the LZSM interferometry have also been studied [32–35]. However, the discussions in previous works have neglected the relationship between this particular loop structure and the nonlinear LZSM interference, which is still an exciting and worthwhile question.

The two-leg ladder system [36–41] is an ideal model to study the influence of orbital magnetic field effects and the nonequilibrium dynamical behavior of bosons or fermions in

the low-dimensional quantum system. This system has also inspired significant research efforts on the quantum Hall effect [42–44], quantum phase transition [45–53], and Hofstadter Hamiltonian [54,55]. Moreover, the ladder system couples the momentum with the magnetic field effect, where different legs can be regarded as the pseudospin, offering an effective way to realize spin-orbit coupling (SOC) [54,56]. The dispersion relation of the system shows a similar two-level structure, which makes it an ideal research platform for studying oscillation and tunneling dynamics. In the presence of a static linear force along the legs, the chiral Bloch oscillation has been observed, which can be used to distinguish quantum phases in the ladder system [57,58]. The detailed discussion on the LZSM interference of this ladder system has shown that the interference phase is closely related to the gauge field, providing a new method to measure artificial gauge fields [59]. However, these studies on the dynamic process of this model mainly focus on the flux ladder system without considering the atomic interaction. The nonlinear effect caused by the atomic interaction in this flux ladder system is still a fascinating and challenging problem. Recently, through microscopic atomic control and detection, the chirality in the propagation dynamics of atoms induced by the atomic interaction in the two-leg ladder system has been observed in the experiment [60]. By using internal spin states or other degrees of freedom to implement the synthetic dimension [61–67], the synthetic flux ladders [42,43,68–70] have been realized in which the long-range interaction in the rung direction could be considered. Therefore, studying the nonlinear LZSM tunneling and interference dynamics in the flux ladder system with complex atomic interactions is a crucial requirement for current experiments and may have significant applications in quantum-mechanical circuits, superconducting qubits, and precision measurements [59,71,72].

\*Corresponding author: [xuejk@nwnu.edu.cn](mailto:xuejk@nwnu.edu.cn)

Considering both on-site and long-range interactions in the rung direction, nonlinear LZSM tunneling dynamics and interference phenomena of the biased two-leg flux ladder driven by an external gravitational field are studied. Using mean-field theory, we derive the dispersion relation of the extended Bose-Hubbard flux ladder system with a nonlinear loop structure. The presence of this loop structure leads to a nonlinear Landau-Zener tunneling process, which reveals the nonlinear energy band characteristics and the unique chirality of the flux ladder system. Because of the periodicity of the energy band structure of the flux ladder system, the nonlinear LZSM interference without Floquet engineering can be easily realized [15,73]. Interestingly, the nonlinear loop structure of the energy band is directly distinguished by the noise of the interference pattern, which establishes a direct link between the nonlinear loop structure and LZSM interferometry. Moreover, the position, intensity, symmetry, and width of the interference pattern are strongly dependent on the magnetic flux, rung-to-leg coupling ratio, energy bias, and effective interaction. This means that these parameters in the flux ladder system can be measured by using nonlinear LZSM interference. Therefore, this paper further extends the study of the flux ladder system to the nonlinear region and provides an effective method for accurate measurement of the system parameters of nonlinear systems.

The paper is organized as follows. In Sec. II, we describe the extended Bose-Hubbard flux ladder model and its nonlinear dispersion relation. The results for nonlinear Landau-Zener tunneling dynamics of the flux ladder system are reported in Sec. III. In Sec. IV, we investigate the nonlinear LZSM interference of the ladder system in four different limiting cases. Finally, the summary and outlook of our paper are included in Sec. V.

## II. MODEL

As realized in the experiment [38], by changing the frequency of a pair of running-wave beams, a controlled energy bias between the two legs of the ladder is introduced, which is effectively analogized to the Zeeman field in SOC systems. When considering the on-site interaction and long-range interaction in the rung direction, complex nonlinear effects can be introduced into the flux ladder system. In solids, the Landau-Zener tunneling effect is usually driven by an external electric field, while in neutral cold atom systems, such external field can be created by using gravity [74–76] or linearly accelerating the lattice [77,78]. To investigate the nonlinear

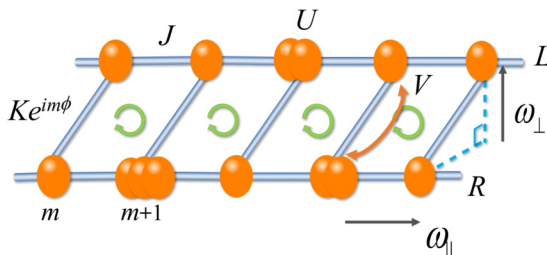


FIG. 1. Schematic diagram of a biased interacting flux ladder system in a gravitational field.

LZSM dynamics of the ladder system, we introduce a gravitational field along the direction of the ladder legs. Then, the Hamiltonian of the system can be written as

$$\begin{aligned}
 H = & -J \sum_m \sum_{\sigma=L,R} (e^{i\frac{\phi}{2}} \hat{a}_{m+1,\sigma}^\dagger \hat{a}_{m,\sigma}) - K \sum_m \hat{a}_{m,R}^\dagger \hat{a}_{m,L} + \text{H.c.} \\
 & + \frac{1}{2} \omega_\perp \sum_m (\hat{a}_{m,L}^\dagger \hat{a}_{m,L} - \hat{a}_{m,R}^\dagger \hat{a}_{m,R}) + \omega_\parallel \sum_m \\
 & \times \sum_{\sigma=L,R} m (\hat{a}_{m,\sigma}^\dagger \hat{a}_{m,\sigma}) + \frac{U}{2} \sum_m \sum_{\sigma=L,R} \hat{a}_{m,\sigma}^\dagger \hat{a}_{m,\sigma}^\dagger \hat{a}_{m,\sigma} \hat{a}_{m,\sigma} \\
 & + V \sum_m \hat{a}_{m,L}^\dagger \hat{a}_{m,R}^\dagger \hat{a}_{m,L} \hat{a}_{m,R}, \quad (1)
 \end{aligned}$$

where the operator  $\hat{a}_{m,\sigma}$  ( $\hat{a}_{m,\sigma}^\dagger$ ) annihilates (creates) a particle at the site  $m$  in the left or right leg ( $\sigma = L$  or  $R$ ). A schematic diagram of this flux ladder with the external field and complex interactions is given in Fig. 1. In the experiment [38], the nearest-neighbor tunneling amplitude along the legs is approximately  $J \approx 150h$  Hz. The tunneling amplitude on rung  $K$  can be controlled by modulating the strength of the laser-assisted tunneling between the legs of the ladder. We use parameter  $J$  as the unit of the energy, and one can obtain that the rung-to-leg coupling ratio is  $\tilde{K} = K/J$ . To study tunneling dynamics, we only focus on the case where the lowest energy band has a double well structure, i.e.,  $0 < \tilde{K} < 1$ . The effective magnetic field  $0 < \phi < 2\pi$  can be tuned by changing the wavelength of the running-wave beams or the angle between them [60]. The strength of the on-site atomic interaction  $U$  and the long-range atomic interaction in the rung direction  $V$  depends on the properties of the atomic species and can be controlled by the lattice modulation [53,79] or Feshbach resonance technologies [80,81]. We consider the reasonable weak interaction strength  $0 < \tilde{U} < 2$  ( $\tilde{U} = U/J$ ) and  $0 < \tilde{V} < 2$  ( $\tilde{V} = V/J$ ).  $\omega_\perp$  is the controllable energy bias between two legs, where  $0 < \tilde{\omega}_\perp < 2$  ( $\tilde{\omega}_\perp = \omega_\perp/J$ ).  $\omega_\parallel$  is the longitudinal in-plane component of a gravitational field, which offers a linear force to drive atoms moving along the energy band. The force generated by gravity can be expressed as  $\omega_\parallel = gM \cos \theta$ , where  $g$  is the gravitational acceleration,  $M$  is the atomic mass, and  $\theta$  is the angle between the lattice and the axis of Earth's gravity [82]. We set  $0 < \tilde{\omega}_\parallel < 1$  ( $\tilde{\omega}_\parallel = \omega_\parallel/J$ ). The value of  $g$  can be measured with high precision using the Bloch oscillation of cold atoms in an optical lattice, providing measurements at the micrometer scale with a sensitivity of ppm [83–85].

We ignore thermal fluctuations with the mean-field approximation  $\hat{a}_{m,\sigma} \simeq \langle \hat{a}_{m,\sigma} \rangle \equiv a_{m,\sigma}$ . By using the Heisenberg equation of motion  $i\hbar \frac{da_{n,\sigma}}{dt} = \frac{\partial H}{\partial a_{n,\sigma}^\dagger}$ , the Gross-Pitaevskii equation of the system can be written as

$$\begin{aligned}
 i\dot{a}_{m,L} = & - (e^{-i\frac{\phi}{2}} a_{m+1,L} + e^{i\frac{\phi}{2}} a_{m-1,L}) - \tilde{K} a_{m,R} + \frac{1}{2} \tilde{\omega}_\perp a_{m,L} \\
 & + \tilde{\omega}_\parallel m a_{m,L} + \tilde{U} |a_{m,L}|^2 a_{m,L} + \tilde{V} |a_{m,R}|^2 a_{m,L}, \\
 i\dot{a}_{m,R} = & - (e^{i\frac{\phi}{2}} a_{m+1,R} + e^{-i\frac{\phi}{2}} a_{m-1,R}) - \tilde{K} a_{m,L} - \frac{1}{2} \tilde{\omega}_\perp a_{m,R} \\
 & + \tilde{\omega}_\parallel m a_{m,R} + \tilde{U} |a_{m,R}|^2 a_{m,R} + \tilde{V} |a_{m,L}|^2 a_{m,R}, \quad (2)
 \end{aligned}$$

where we use the natural unit  $\hbar = 1$ . When the longitudinal gravitational field is not considered ( $\tilde{\omega}_\parallel = 0$ ), the system has

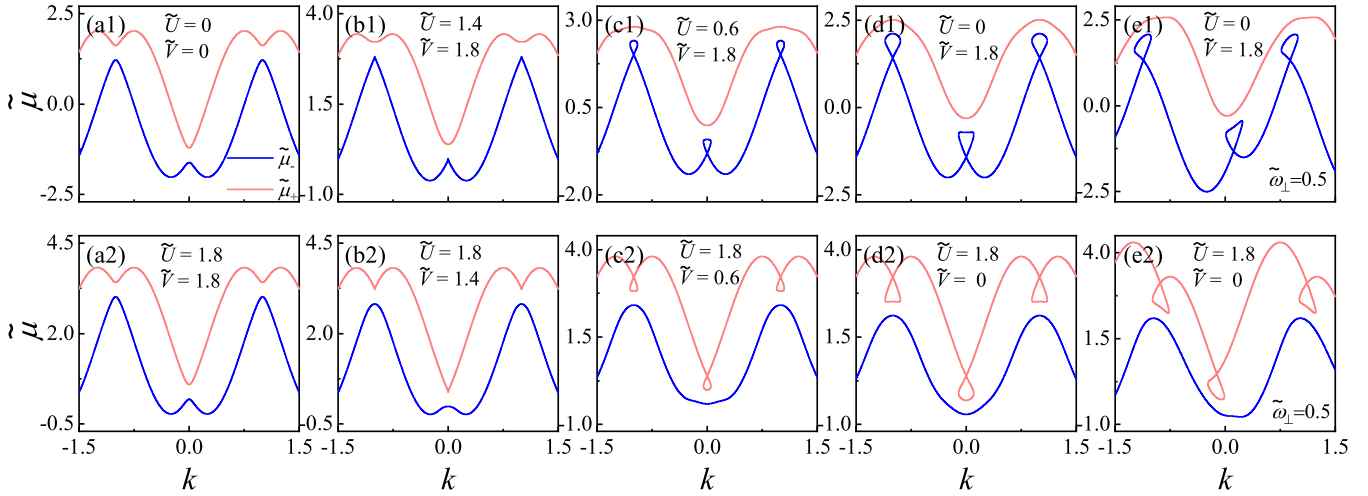


FIG. 2. Dispersion relations of the biased interacting flux ladder system for the case (a1) without interaction  $\tilde{U} = \tilde{V} = 0$ , (a2) with equal on-site interaction and long-range interaction in the rung direction  $\tilde{U} = \tilde{V} = 1.8$ , (b1–e1) with large long-range interaction in the rung direction  $\tilde{U} < \tilde{V}$ , and (b2–e2) with large on-site interaction  $\tilde{U} > \tilde{V}$ . The other parameters are  $\tilde{K} = 0.2$  and  $\phi = 0.5\pi$ .

plane-wave solutions  $a_{m,\sigma} = a_\sigma(t)e^{ikm}$ , where  $k$  is the quasi-momentum, which is rescaled as  $k \rightarrow kd/\pi$  ( $d$  is the lattice constant). Substituting it into Eq. (2), the dynamic equation in the momentum space can be obtained:

$$\begin{aligned} i\dot{a}_L &= -2 \cos\left(k - \frac{\phi}{2}\right)a_L - \tilde{K}a_R + \frac{1}{2}\tilde{\omega}_\perp a_L \\ &\quad + \tilde{U}|a_L|^2 a_L + \tilde{V}|a_R|^2 a_L, \\ i\dot{a}_R &= -2 \cos\left(k + \frac{\phi}{2}\right)a_R - \tilde{K}a_L - \frac{1}{2}\tilde{\omega}_\perp a_R \\ &\quad + \tilde{U}|a_R|^2 a_R + \tilde{V}|a_L|^2 a_R. \end{aligned} \quad (3)$$

Setting  $a_\sigma(t) = \tilde{a}_\sigma e^{-i\tilde{\mu}t}$ , where  $\tilde{a}_\sigma$  is the time-independent wave function and  $\tilde{\mu}$  is the chemical potential, which is rescaled as  $\tilde{\mu} \rightarrow \mu/J$ , we have the corresponding stationary state equation:

$$\begin{aligned} \tilde{\mu}\tilde{a}_L &= -2 \cos\left(k - \frac{\phi}{2}\right)\tilde{a}_L - \tilde{K}\tilde{a}_R + \frac{1}{2}\tilde{\omega}_\perp\tilde{a}_L \\ &\quad + \tilde{U}|\tilde{a}_L|^2\tilde{a}_L + \tilde{V}|\tilde{a}_R|^2\tilde{a}_L, \\ \tilde{\mu}\tilde{a}_R &= -2 \cos\left(k + \frac{\phi}{2}\right)\tilde{a}_R - \tilde{K}\tilde{a}_L - \frac{1}{2}\tilde{\omega}_\perp\tilde{a}_R \\ &\quad + \tilde{U}|\tilde{a}_R|^2\tilde{a}_R + \tilde{V}|\tilde{a}_L|^2\tilde{a}_R. \end{aligned} \quad (4)$$

According to Eq. (4) and the normalization condition  $|\tilde{a}_L|^2 + |\tilde{a}_R|^2 = 1$ , we can obtain the nonlinear dispersion relation of the system.

As shown in Fig. 2, the energy band of the biased interacting flux ladder system consists of an upper band (red) and a lower band (blue). When the strength of the on-site interaction is equal to the long-range interaction in the rung direction, i.e., the effective interaction is zero [Fig. 2(a2)], the shape of the energy band is consistent with the linear case without interaction [Fig. 2(a1)], but the corresponding energy values are different, i.e., the energy band is just a displacement upwards of the linear case. As the strength of the

effective interaction increases, the energy band structure of the system becomes more complex, exhibiting a loop structure. In order to describe this phenomenon analytically, we use  $\tilde{\mu}_{\text{non}} = \tilde{\mu} + 2 \cos k \cos \frac{\phi}{2} + \frac{\tilde{U} + \tilde{V}}{2}(|\tilde{a}_L|^2 + |\tilde{a}_R|^2)$  and simplify Eq. (4) to the standard nonlinear equation form

$$\begin{aligned} \tilde{\mu}_{\text{non}}\tilde{a}_L &= \left[ -2 \sin k \sin \frac{\phi}{2} + \frac{\tilde{\omega}_\perp}{2} - \frac{\tilde{U} - \tilde{V}}{2}(|\tilde{a}_R|^2 - |\tilde{a}_L|^2) \right] \tilde{a}_L \\ &\quad - \tilde{K}\tilde{a}_R, \\ \tilde{\mu}_{\text{non}}\tilde{a}_R &= \left[ 2 \sin k \sin \frac{\phi}{2} - \frac{\tilde{\omega}_\perp}{2} + \frac{\tilde{U} - \tilde{V}}{2}(|\tilde{a}_R|^2 - |\tilde{a}_L|^2) \right] \tilde{a}_R \\ &\quad - \tilde{K}\tilde{a}_L. \end{aligned} \quad (5)$$

Similar to the classical two-level model [23,24,28], when the nonlinear term  $\frac{\tilde{U} - \tilde{V}}{2}(|\tilde{a}_R|^2 - |\tilde{a}_L|^2)$  dominates over the energy gap term  $\tilde{K}$ , a loop structure appears in the energy band. As shown in Figs. 2(b1) and 2(b2), when  $|\tilde{U} - \tilde{V}| = 2\tilde{K}$ , a cusp appears at the avoided crossing, located in the upper (lower) energy band for attractive effective interactions  $\tilde{U} < \tilde{V}$  (repulsive effective interactions  $\tilde{U} > \tilde{V}$ ). With the increase of the strength of the effective interaction  $|\tilde{U} - \tilde{V}|$ , i.e., the nonlinear effect, a loop structure appears in the energy band, and the size of the loop is positively associated with the strength of the effective interaction [see Figs. 2(c1)–2(d2)]. Significantly, since the energy band of the flux ladder system exhibits a periodic structure, the loop structure will appear at  $k = n\pi$  ( $n = 0, \pm 1, \pm 2, \dots$ ). Because the flux ladder system has both the essence of the SOC system and periodic energy band structure, it provides an ideal platform for investigating the LZSM interference phenomenon without complex Floquet engineering. When the strength of the effective interaction is large, the shapes of loops are different with odd  $n$  and even  $n$ , respectively. According to Eq. (5), we can analytically calculate the edge of

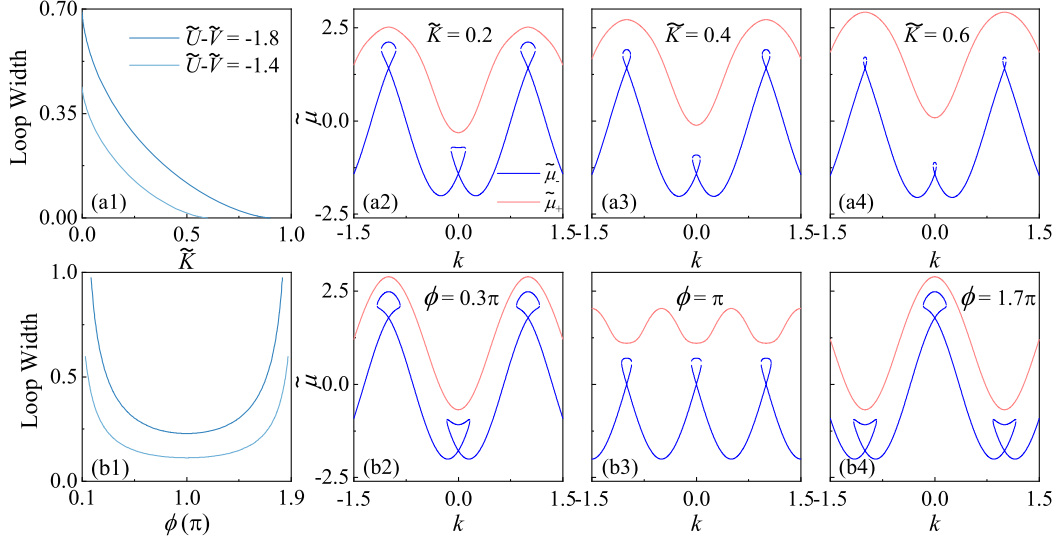


FIG. 3. (a1) Loop widths as the function of the rung-to-leg coupling ratio  $\tilde{K}$  with different effective interaction strength. Corresponding energy band structures for different rung-to-leg coupling ratios (a2)  $\tilde{K} = 0.2$ , (a3)  $\tilde{K} = 0.4$ , and (a4)  $\tilde{K} = 0.6$  with  $\tilde{U} - \tilde{V} = -1.8$  and  $\phi = 0.5\pi$ . (b1) Loop widths as the function of the magnetic flux  $\phi$  with different effective interaction strength. Corresponding energy band structures for different fluxes (b2)  $\phi = 0.3\pi$ , (b3)  $\phi = \pi$ , and (b4)  $\phi = 1.7\pi$  with  $\tilde{U} - \tilde{V} = -1.8$  and  $\tilde{K} = 0.2$ .

the loop:

$$k_e = \pm \arcsin \left\{ \frac{\tilde{K}}{2 \sin \frac{\phi}{2}} \left[ \left( \frac{\tilde{U} - \tilde{V}}{2\tilde{K}} \right)^{\frac{2}{3}} - 1 \right]^{\frac{3}{2}} \right\} \pm \arcsin \left( \frac{\tilde{\omega}_{\perp}}{4 \sin \frac{\phi}{2}} \right) + n\pi, \quad (6)$$

where  $k_c = \pm \arcsin\left(\frac{\tilde{\omega}_{\perp}}{4 \sin \frac{\phi}{2}}\right)$  is the center of the loop, which is nonzero when the energy bias between two legs is considered [see Figs. 2(e1) and 2(e2)]. Then, the loop width  $2|k_e - k_c|$  as the function of the rung-to-leg coupling ratio  $\tilde{K}$  and the magnetic flux  $\phi$  are plotted in Figs. 3(a1) and 3(b1), respectively. As shown in Figs. 3(a2)–3(a4), the loop width decreases and the energy gap between two bands increases with the increasing rung-to-leg coupling ratio. Interestingly, the structure of the nonlinear dispersion relation changes dramatically with different magnetic fluxes, and there is a minimum value of the loop width when the magnetic flux  $\phi = \pi$  [see Figs. 3(b1)–3(b4)].

### III. NONLINEAR LANDAU-ZENER TUNNELING DYNAMICS

To investigate the nonlinear Landau-Zener tunneling dynamics of the biased interacting flux ladder system, we introduce a gravitational field along the direction of the leg. This field tilts the optical lattice and induces Bloch oscillations, Landau-Zener tunneling, and LZSM interferometry of the atoms. By setting the initial quasimomentum as  $k = k_0$ , the dynamics of the quasimomentum follows the classical acceleration  $k(t) = k_0 + \tilde{\omega}_{\parallel}t$ . In analogy with a standard nonlinear two-level model, the dynamic equation in the

momentum space is given:

$$\begin{aligned} i\dot{a}_L &= \left[ \frac{\tilde{\omega}_{\perp} - 4 \sin \frac{\phi}{2} \sin(k_0 + \tilde{\omega}_{\parallel}t)}{2} \right. \\ &\quad \left. - \frac{\tilde{U} - \tilde{V}}{2} (|a_R|^2 - |a_L|^2) \right] a_L - \tilde{K} a_R, \\ i\dot{a}_R &= - \left[ \frac{\tilde{\omega}_{\perp} - 4 \sin \frac{\phi}{2} \sin(k_0 + \tilde{\omega}_{\parallel}t)}{2} \right. \\ &\quad \left. + \frac{\tilde{U} - \tilde{V}}{2} (|a_R|^2 - |a_L|^2) \right] a_R - \tilde{K} a_L, \end{aligned} \quad (7)$$

where  $4 \sin \frac{\phi}{2} \sin(k_0 + \tilde{\omega}_{\parallel}t)$  is the driving term generated by the gravitational field,  $4 \sin \frac{\phi}{2}$  is the driving amplitude,  $\tilde{\omega}_{\parallel}$  is the driving force, and  $k_0$  is the initial momentum.

Figure 4 shows the nonlinear Landau-Zener tunneling dynamics of the system when the energy band exhibits the loop structure. We use the fourth-order Runge-Kutta method [86], which is a useful numerical integration algorithm for solving the ordinary differential equations, to solve Eq. (7) with the time step  $t_h = 0.0005$ . Here, for the initial momentum  $k_0$ , the initial states  $a_L(0)$  and  $a_R(0)$  are determined by the momentum and eigenstates corresponding to the points  $B_{\pm}$  or  $C_{\pm}$  marked in Fig. 4, which are given by Eq. (4). The loop structure appears in the lower energy band when the effective interaction is repulsive  $\tilde{U} > \tilde{V}$ . The points  $B_{\pm}$  [the blue square in Fig. 4(a1)] and  $C_{\pm}$  [the red dots in Fig. 4(a1)] are set as initial states, and Figs. 4(b1) and 4(c1) describe the corresponding nonlinear Landau-Zener tunneling with a weak driving force  $\tilde{\omega}_{\parallel} = 0.005$ , respectively. When the initial state is in the upper band  $B_+$  ( $C_+$ ), there is no loop structure on the energy band, so the atoms will move smoothly along the



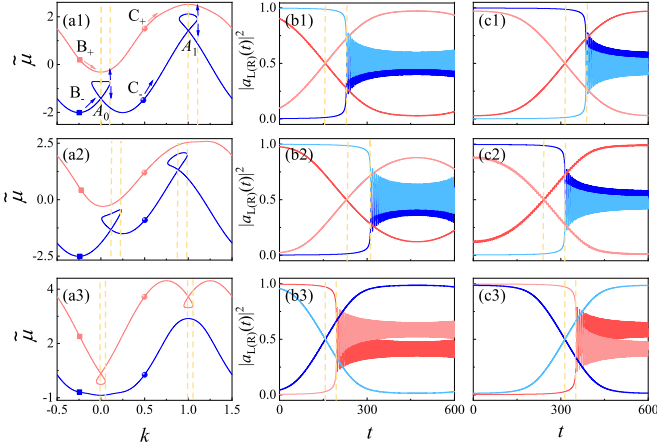


FIG. 4. Nonlinear Landau-Zener tunneling dynamics for different dispersion relations of the biased interacting flux ladder system (a1)  $\tilde{U} = 0 < \tilde{V} = 1.8$  and  $\tilde{\omega}_\perp = 0$ , (a2)  $\tilde{U} = 0 < \tilde{V} = 1.8$  and  $\tilde{\omega}_\perp = 0.5$ , and (a3)  $\tilde{U} = 1.8 > \tilde{V} = 0$  and  $\tilde{\omega}_\perp = 0$ . The second (third) column shows the tunneling dynamics of the system starting from  $B_\pm$  ( $C_\pm$ ) points, where red and blue lines indicate the atoms starting from the upper and lower bands, respectively. Dark (light) color lines correspond to the population probability  $|a_{L(R)}(t)|^2$  for the left (right) leg momentum state. The other parameters are  $\tilde{K} = 0.2$ ,  $\tilde{\omega}_\parallel = 0.005$  and  $\phi = 0.5\pi$ .

upper band and gradually exchange their spin states, which are the left and right momentum states in the ladder system. The atoms arriving at the avoided crossing  $A_0$  ( $A_1$ ) will have identical distributions on the left and right momentum states [see Figs. 4(b1) and 4(c1)]. When the initial state is in the lower band  $B_-$  ( $C_-$ ), the atoms do not tunnel at  $A_0$  ( $A_1$ ) due to the presence of the loop structure, and the nonlinear Landau-Zener tunneling occurs until it reaches the loop boundary. As shown by the blue curves in Figs. 4(b1) and 4(c1), the left and right momentum states hold onto the initial distribution until the atoms reach the loop boundary, where a significant exchange between the upper and lower energy bands occurs, characterized by the high-frequency nonlinear oscillation between the two momentum states. The distance between the equal left and right momentum state distribution and the nonlinear Landau-Zener tunneling, i.e., the distance between the two vertical yellow lines in Figs. 4(b1) and 4(c1), corresponds to half of the loop width. Comparing Figs. 4(b1) and 4(c1) one finds that although the corresponding loop structures have different shapes, the loop width does not depend on the initial position of the atoms and the loop shape. More interestingly, when atoms initially are in the first half period of the energy band, they mainly occupy the left momentum state of the ladder system in the upper band while mainly occupying the right momentum state of the ladder system in the lower band. A reverse situation can be observed during the second half period of the energy band. This distribution characteristic results in the spin-momentum locking of the SOC effect and reflects the flux ladder system's unique chirality features.

The energy band structure of the system is no longer symmetric [see Fig. 4(a2)] when the energy bias between the two legs of the ladder is considered. Positions of the equal

left and right momentum state distribution and the nonlinear Landau-Zener tunneling are shifted. At the same time, their distance, i.e., the distance between the two vertical yellow lines in Figs. 4(b2) and 4(c2), is kept unchanged. The energy bias between the two legs of the ladder only changes the loop structure, which is compatible with the result given by Eq. (6). As shown in Fig. 4(a3), the loop structure appears in the upper energy band when the effective interaction is attractive  $\tilde{U} < \tilde{V}$ . Thus, the nonlinear Landau-Zener tunneling occurs when the initial state is in the upper band [see red lines in Figs. 4(b3) and 4(c3)], and the smooth exchange of momentum states occurs when the initial state is in the lower band [see blue lines in Figs. 4(b3) and 4(c3)]. Moreover, the width of the loop and the distance between the two vertical yellow lines decrease with decreasing the effective interaction strength. Therefore, nonlinear Landau-Zener tunneling dynamics can provide an efficient way to measure the loop structure of the energy band in the experiment and makes it possible to measure the magnitude of the system's nonlinear effect quantitatively.

In order to describe the nonlinear Landau-Zener tunneling more comprehensively, we investigate the variation of the tunneling probability with different parameters when the initial state is in the energy band with a loop structure. In the nonadiabatic region near the avoided crossing  $A_n$  of the energy band,  $t = t_{A_n} + \tau$  with  $\tilde{\omega}_\parallel |\tau| \ll 1$ , Eq. (7) can be written as

$$\begin{aligned} i\dot{a}_L &= \left[ \frac{\alpha t}{2} - \frac{\tilde{U} - \tilde{V}}{2} (|a_R|^2 - |a_L|^2) \right] a_L - \tilde{K} a_R, \\ i\dot{a}_R &= - \left[ \frac{\alpha t}{2} + \frac{\tilde{U} - \tilde{V}}{2} (|a_R|^2 - |a_L|^2) \right] a_R - \tilde{K} a_L, \end{aligned} \quad (8)$$

where

$$\alpha = 4 \sin \frac{\phi}{2} \tilde{\omega}_\parallel \sqrt{1 - \left( \frac{\tilde{\omega}_\perp}{4 \sin \frac{\phi}{2}} \right)^2}. \quad (9)$$

Then, the tunneling probability  $\Gamma$  can be estimated theoretically [23]. When  $|\tilde{U} - \tilde{V}| \gg 2\tilde{K}$ , the tunneling probability  $\Gamma$  is found to be

$$\begin{aligned} \Gamma &= 1 - |a_{R(L)}|_{-\infty}^2 = 1 - \tilde{K}^2 \left| \int_{-\infty}^{+\infty} dt e^{-\frac{i}{2}\tilde{\alpha}(t-t_0)^2} \right|^2 \\ &= 1 - \frac{2\pi\tilde{K}^2}{\tilde{\alpha}}, \end{aligned} \quad (10)$$

with

$$\tilde{\alpha} = \alpha \pm (\tilde{U} - \tilde{V})\tilde{K}^2 \sqrt{\frac{\pi}{\tilde{\alpha}}}. \quad (11)$$

Here, for the repulsive effective interaction the atoms are almost all concentrated in the left momentum state initially, the tunneling probability is  $1 - |a_R|_{-\infty}^2$ , and Eq. (11) takes a positive sign. Conversely, when the effective interaction is attractive, the situation is reversed. Then the above result yields a closed equation for the  $\Gamma$ :

$$\frac{1}{1 - \Gamma} = \frac{1}{P} \pm \frac{\tilde{U} - \tilde{V}}{\sqrt{2\pi}\tilde{K}} \sqrt{1 - \Gamma}. \quad (12)$$

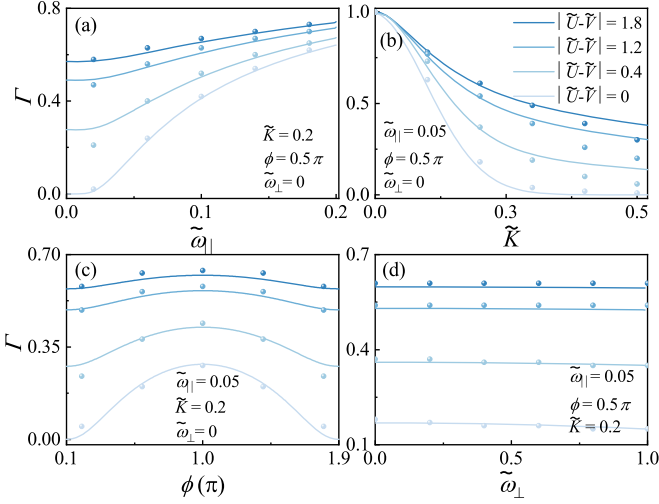


FIG. 5. Nonlinear Landau-Zener tunneling probability  $\Gamma$  as the function of (a) the gravitational field  $\tilde{\omega}_{||}$ , (b) rung-to-leg coupling ratio  $\tilde{K}$ , (c) magnetic flux  $\phi$ , and (d) energy bias  $\tilde{\omega}_{\perp}$  for different effective interaction  $|\tilde{U} - \tilde{V}|$ .

Here, we take the quantity

$$P = 1 - \exp\left(-\frac{2\pi\tilde{K}^2}{\alpha}\right), \quad (13)$$

and then the result can be extended to a wide range of the effective interaction strength. Equations (9)–(13) indicate that  $\phi$ ,  $\tilde{K}$ ,  $|\tilde{U} - \tilde{V}|$ ,  $\tilde{\omega}_{||}$ , and  $\tilde{\omega}_{\perp}$  have coupled effects on the tunneling probability of the nonlinear Landau-Zener tunneling of the ladder system.

We plot the tunneling probability  $\Gamma$  as the function of the gravitational field  $\tilde{\omega}_{||}$ , rung-to-leg coupling ratio  $\tilde{K}$ , magnetic flux  $\phi$ , and energy bias  $\tilde{\omega}_{\perp}$  in Fig. 5. Both the theoretical results given by Eq. (12) and numerical simulations of Eq. (7) are presented. In the ladder system, the gravitational field  $\tilde{\omega}_{||}$  plays a role as the driving force, thus the tunneling probability increases with the increase of  $\tilde{\omega}_{||}$  [see Fig. 5(a)]. Note that the presence of nonlinear interaction terms means that the tunneling probability is not zero in the adiabatic limit  $\tilde{\omega}_{||} \rightarrow 0$ . As shown in Fig. 5(b), with the increase of the coupling ratio  $\tilde{K}$ , the energy gap between two bands increases, thus the tunneling probability between two bands decreases, while the increase of the effective interaction strength enlarges the size of the loop structure, effectively facilitating Landau-Zener tunneling in the ladder system. Interestingly, Fig. 5(c) reveals that there is the maximum tunneling probability when the magnetic flux  $\phi = \pi$ , which seems to contradict the conclusion that the large loop size accompanies the large tunneling probability. This can be understood according to Eq. (9); the magnetic flux can modulate the strength of the driving force  $\tilde{\omega}_{||}$  with the form of  $\sin \frac{\phi}{2}$ , which is the largest at  $\phi = \pi$ .

Therefore, the magnetic field and the driving force have coupled effects on the tunneling probability, providing a way to manipulate the tunneling probability in the flux ladder system. Figure 5(d) shows that the tunneling probability slightly decreases as the energy bias increases.

#### IV. NONLINEAR LZSM INTERFEROMETRY

Due to the periodic structure of the dispersion relation of the flux ladder system (see Figs. 2–4), the atoms can periodically pass through the avoided crossing region under the driving of the gravitational field, which will cause the LZSM interference. This quantum interference phenomenon has attracted considerable theoretical and experimental studies, with a particular focus on accurate measurement. In the case of biased ladder systems considered here, the presence of complex interactions and corresponding energy band structures leads to evident nonlinear effects in this interference phenomenon. Moreover, the left-right leg degree of freedom in this ladder can be regarded as a pseudospin, which provides an efficient path to implement one-dimensional SOC. Therefore, the flux ladder system offers an ideal playground to realize the nonlinear LZSM interference without complex Floquet engineering on the spin-orbit band [73]. The dynamic equation in the momentum space of the ladder system can be described by Eq. (7). Subsequently, we will discuss nonlinear effects of LZSM interference in the ladder system under four different limiting cases.

##### A. Weak coupling limit

First, we consider the interference process of the biased flux ladder system in the weak coupling limit ( $\tilde{K} \ll \tilde{\omega}_{||}$ ). In this case, the coupling between the two energy states of the system is much smaller than the driving force, so the energy levels at the cross points of the energy bands are almost degenerate, and the tunneling between the two momentum states is very weak and almost negligible, i.e.,  $|a_{\sigma}(t)|^2 \simeq |a_{\sigma}(t_0)|^2$ . For the initial state  $a_L(t_0) = 0$ ,  $a_R(t_0) = 1$ ,  $k_0 = 0$ , we use the variable transformation

$$a_{\sigma}(t) = a'_{\sigma}(t) \exp \left\{ \pm i \left[ \frac{\tilde{\omega}_{\perp}}{2} t + \frac{2 \cdot \sin \frac{\phi}{2} \cos \tilde{\omega}_{||} t}{\tilde{\omega}_{||}} - \frac{(\tilde{U} - \tilde{V})(|a_R(t_0)|^2 - |a_L(t_0)|^2)}{2} t \right] \right\}. \quad (14)$$

Then, Eq. (7) can be reduced to the linear form

$$\begin{aligned} i\dot{a}'_L(t) &= -\tilde{K}e^{i\theta(t)}a'_R(t), \\ i\dot{a}'_R(t) &= -\tilde{K}e^{-i\theta(t)}a'_L(t), \end{aligned} \quad (15)$$

where

$$\theta(t) = \tilde{\omega}_{\perp} t + \frac{4 \cdot \sin \frac{\phi}{2} \cos \tilde{\omega}_{||} t}{\tilde{\omega}_{||}} - (\tilde{U} - \tilde{V})t \quad (16)$$

is the relative phase between the two adiabatic states. For a complete LZSM interference cycle, the accumulated relative phase is approximately equal to

$$\theta_d \simeq \int_{t_{A_0}}^{t_{A_0} + \frac{2\pi}{\tilde{\omega}_{||}}} \theta(t) dt = \frac{2\pi}{\tilde{\omega}_{||}} [\tilde{\omega}_{\perp} - (\tilde{U} - \tilde{V})], \quad (17)$$

where the avoided crossings occur at times  $t_{A_0, A_1} + 2n\pi/\tilde{\omega}_{||}$ ,  $\tilde{\omega}_{||}t_{A_0} = \arcsin(\tilde{\omega}_{\perp}/4 \sin \frac{\phi}{2})$ ,  $\tilde{\omega}_{||}t_{A_1} = \pi - \tilde{\omega}_{||}t_{A_0}$ .  $t_{A_0, A_1}$  is the time of passing through  $A_0, A_1$  of the energy band [see Fig. 4(a1)].

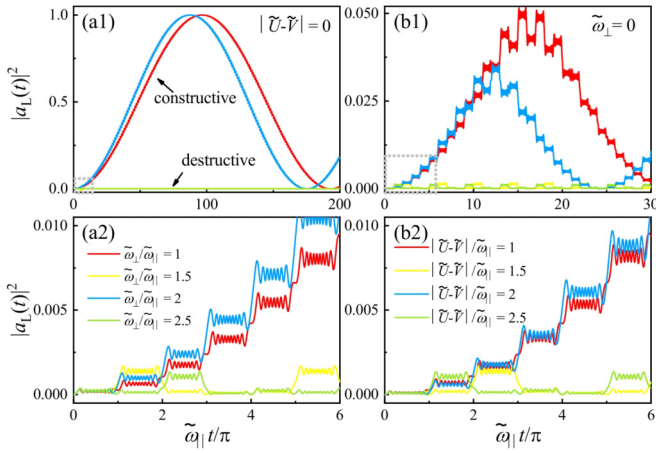


FIG. 6. Time evolutions of the population probability  $|a_L(t)|^2$  for the left leg momentum state in the weak coupling limit with (a1) zero effective interaction  $|\tilde{U} - \tilde{V}| = 0$  and different energy biases and (b1) zero energy bias  $\tilde{\omega}_\perp = 0$  and different effective interactions. (a2) and (b2) show magnified views of boxed areas in (a1) and (b1), respectively. The other parameter are  $\phi = 0.5\pi$ ,  $\tilde{K}/\tilde{\omega}_\parallel = 0.1$ .

As shown in Fig. 6, when  $\theta_d \simeq 2n\pi$ , that is,  $\tilde{\omega}_\perp - (\tilde{U} - \tilde{V}) = n\tilde{\omega}_\parallel$ , a constructive interference pattern occurs (see red and blue curves in Fig. 6). When  $\theta_d \simeq (2n + 1)\pi$ , that is,  $\tilde{\omega}_\perp - (\tilde{U} - \tilde{V}) = (n + \frac{1}{2})\tilde{\omega}_\parallel$ , a destructive interference pattern takes place (see yellow and green curves in Fig. 6). In Figs. 6(a1) and 6(a2), where the effective interaction strength  $|\tilde{U} - \tilde{V}| = 0$ , the interference pattern of the system is determined by the energy bias. For the constructive interference, the population probability  $|a_L(t)|^2$  for the left leg momentum state exhibits staged growth within a short time and periodic behavior over a longer duration. For the destructive interference, the population probability only shows small fluctuations over time. When the energy bias  $\tilde{\omega}_\perp = 0$ , the interference pattern of the system is determined by the effective interaction strength  $|\tilde{U} - \tilde{V}|$  [see Figs. 6(b1) and 6(b2)]. In this case, the oscillation period and amplitude of the population probability  $|a_L(t)|^2$  for the left leg momentum state are significantly reduced in the case of constructive interference. Interestingly, the presence of nonlinear effects in the constructive interference leads to the amplitude of the population probability depending on the effective interaction strength.

### B. Strong coupling limit

Next, we consider the interference process of the biased flux ladder system in the strong coupling limit ( $\tilde{K} \gg \tilde{\omega}_\parallel$ ). In this case, the driving force is sufficiently small, and the system approximates adiabatic evolution, so the tunneling between the two energy bands becomes weak and almost negligible. In the nonadiabatic region near the avoided crossing of the energy band, where  $\tilde{\omega}_\parallel|\tau| \ll 1$ , Eq. (7) can be linearized as Eq. (8). The evolution results of these two equations are consistent from  $t_0 = t_{A_0} - 0.02/\tilde{\omega}_\parallel$  to  $t = t_{A_0} + 0.02/\tilde{\omega}_\parallel$ . As the magnetic flux  $\phi \rightarrow 0$ , Eq. (7) coincides with the double-well model [87]. The system will have an obvious macroscopic self-trapping phenomenon with a large repulsive interaction,

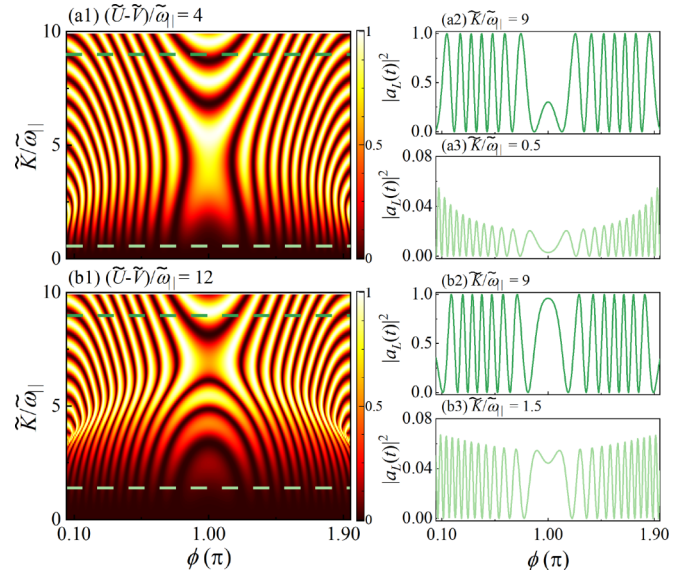


FIG. 7. In the strong coupling limit, LZSM interference patterns on the  $(\phi, \tilde{K}/\tilde{\omega}_\parallel)$  plane with (a1)  $(\tilde{U} - \tilde{V})/\tilde{\omega}_\parallel = 4$  and (b1)  $(\tilde{U} - \tilde{V})/\tilde{\omega}_\parallel = 12$ , respectively. (a2, a3, b2, b3) Corresponding population probability  $|a_L(t)|^2$  for the left leg momentum state at different coupling ratios  $\tilde{K}/\tilde{\omega}_\parallel$ . The other parameter is  $\tilde{\omega}_\perp/\tilde{\omega}_\parallel = 2$ .

and there exists a critical value  $\tilde{K}_c = (\tilde{U} - \tilde{V})/4$  [88,89]. This critical value will offset when the magnetic flux  $\phi \neq 0$ .

As shown in Fig. 7, interference patterns on the  $(\phi, \tilde{K}/\tilde{\omega}_\parallel)$  plane are displayed for the initial state  $a_L(t_0) = 0$ ,  $a_R(t_0) = 1$ , and  $k_0 = 0$ , with the double-passage process from  $t_0 = t_{A_0}$  to  $t = t_{A_1}$ , i.e., the avoided crossing region is passed twice. The interference pattern comprises bright and dark fringes with the magnetic field and is symmetric with respect to  $\phi = \pi$ . In the case with  $(\tilde{U} - \tilde{V})/\tilde{\omega}_\parallel = 4$ , there is a critical value  $\tilde{K}_c \approx 1$  at  $\phi \rightarrow 0$  [see Fig. 7(a1)], which increases as  $\phi$  increases, maximizes when  $\phi = \pi$ , and then decreases. In Fig. 7(a2), the effective interaction energy is less than the energy gap when  $\tilde{K}/\tilde{\omega}_\parallel \gg 1$ , leading to the Josephson oscillations between the two momentum states. The population probability  $|a_L(t)|^2$  oscillates with the magnetic field except for the case  $\phi = \pi$ , where the amplitude of the oscillation is 1. Since the interference pattern strongly depends on the magnetic flux (for example, the zeroth-order fringe corresponds to  $\phi = \pi$ ), the order of the interference fringes can identify the strength of the magnetic field in the ladder system with complex interactions. The effective interaction energy is larger than the energy gap when  $\tilde{K}/\tilde{\omega}_\parallel < 1$ . As shown in Fig. 7(a3), the amplitude of the population probability  $|a_L(t)|^2$  is less than 0.1, indicating that the macroscopic self-trapping phenomenon occurs, i.e., the atoms are mainly concentrated on the right leg momentum state. Moreover, the amplitude of this oscillation decreases with increasing the value of  $\phi$  and maximizes at  $\phi = \pi$ , then decreases. Therefore, the amplitude of this oscillation relies on the magnetic field, which offers a way to measure the magnetic field accurately by using the nonlinear LZSM interference (for example, the amplitude is minimized at  $\phi = \pi$ ). When the effective interaction strength increases, the critical position for the emergence of the macroscopic self-trapping phenomenon increases. In Figs. 7(b1)–7(b3), there is a critical value  $\tilde{K}_c \approx 3$  at  $\phi \rightarrow 0$



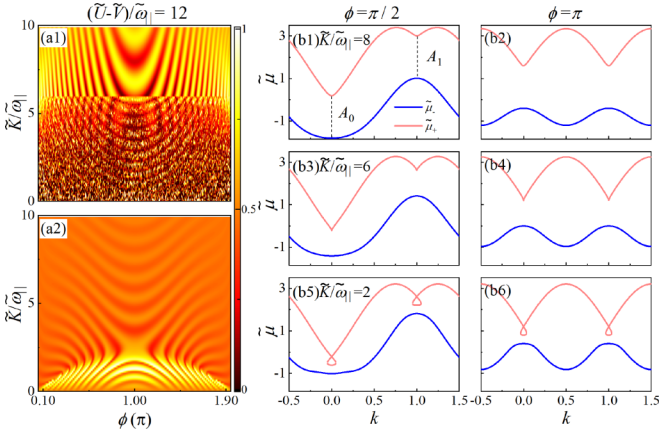


FIG. 8. In the strong coupling limit, LZSM interference patterns on the  $(\phi, \tilde{K}/\tilde{\omega}_{\parallel})$  plane for the atoms are initially in (a1) the upper and (a2) lower band, respectively. Corresponding energy band structures for different magnetic fluxes and coupling ratios with (b1, b2)  $2\tilde{K} > \tilde{U} - \tilde{V}$  (no loop structure), (b3, b4)  $2\tilde{K} = \tilde{U} - \tilde{V}$  (a cusp appears in the energy band), and (b5, b6)  $2\tilde{K} < \tilde{U} - \tilde{V}$  (loop structure appears). The other parameters are  $\tilde{\omega}_{\perp}/\tilde{\omega}_{\parallel} = 2$  and  $(\tilde{U} - \tilde{V})/\tilde{\omega}_{\parallel} = 4$ .

when  $(\tilde{U} - \tilde{V})/\tilde{\omega}_{\parallel} = 12$ . In this sense, the critical location in the interference pattern where self-trapping occurs can precisely measure the effective interaction strength in the ladder system. As shown in Figs. 7(a1) and 7(b1), the strength of the effective interaction can be calculated using the critical value  $\tilde{K}_c = (\tilde{U} - \tilde{V})/4$  where the self-trapping occurs. As discussed above, the interference pattern in the strong coupling limit can reveal the strength of the effective interaction of the ladder system. However, the impact of the interesting loop structure on the interference pattern is still not clear. To consider this impact, we need to prepare the initial state as eigenstates of the system. In Figs. 8(a1) and 8(a2), we show the interference pattern on the  $(\phi, \tilde{K}/\tilde{\omega}_{\parallel})$  plane for the case when the atoms are initially in the upper band and lower band eigenstates, respectively. As depicted in Figs. 8(b1) and 8(b2), no loop structure exists in the energy band, and both kinds of initial distributions

have an interference pattern when  $2\tilde{K} < \tilde{U} - \tilde{V}$  [see upper parts of Figs. 8(a1) and 8(a2)]. However, in Figs. 8(b3)–8(b6), as the coupling ratio  $\tilde{K}$  decreases, a loop structure appears gradually in the upper band. Due to the existence of the loop structure, there exist two kinds of eigenstates with degenerate energy eigenvalues and different momentum state distributions at  $k = A_0$  in the upper band. The noise in the lower part of Fig. 8(a1) is generated by the random initial distribution of the two degenerated eigenstates at the intersection of the loop and the corresponding energy band. The critical position for the emergence of the noise in the interference pattern corresponds to the threshold when a cusp appears in the energy band, i.e.,  $\tilde{K}/\tilde{\omega}_{\parallel} = 6$ . Therefore, the noise in the interference pattern can be used to judge whether a loop structure exists in the corresponding energy band. The critical position where the noise occurs effectively corresponds to the appearance of the cusp in the energy band structure.

### C. Weak driving limit

The Jacobi-Anger relationship  $e^{ix \cos \omega t} = \sum_{j=-\infty}^{\infty} J_j(x)(\pm i)^j e^{\pm i j \omega t}$  can be applied to the weak driving limit  $4 \sin \frac{\phi}{2} \ll \tilde{\omega}_{\parallel}$ , where  $J_j(x)$  is the first kind  $j$ th-order Bessel function with parameter  $x$ . Equation (7) can be greatly simplified by using high-frequency approximation. Due to the small contribution of the higher-order Bessel function, we take only the zeroth-order term into account. Then, Eq. (7) can be deduced to

$$\begin{aligned} i\dot{a}'_L(t) &= -\tilde{K}J_0\left(\frac{4 \sin \frac{\phi}{2}}{\tilde{\omega}_{\parallel}}\right) e^{i[\tilde{\omega}_{\perp} - (\tilde{U} - \tilde{V})]t} a'_R(t), \\ i\dot{a}'_R(t) &= -\tilde{K}J_0\left(\frac{4 \sin \frac{\phi}{2}}{\tilde{\omega}_{\parallel}}\right) e^{-i[\tilde{\omega}_{\perp} - (\tilde{U} - \tilde{V})]t} a'_L(t). \end{aligned} \quad (18)$$

Therefore, when  $\tilde{K}/\tilde{\omega}_{\parallel} \rightarrow 0$ , the peaks of the resonances of the LZSM interference are located at  $\tilde{\omega}_{\perp} - (\tilde{U} - \tilde{V}) = 0$  in the biased flux ladder system. As shown in Fig. 9, interference patterns of the ladder system on the  $(\tilde{K}/\tilde{\omega}_{\parallel}, \tilde{\omega}_{\perp}/\tilde{\omega}_{\parallel})$  plane are displayed by numerical simulations of Eq. (7). When considering the noninteracting ladder system (or the system with the effective interaction  $|\tilde{U} - \tilde{V}| = 0$ ), interference patterns exhibit axisymmetrically about  $\tilde{\omega}_{\perp} = 0$ . For the case where  $\tilde{\omega}_{\perp} = 0$ , we observe that destructive interference fringes always occur at  $2\tilde{K} = n\tilde{\omega}_{\parallel}$ , which is a consequence of multiphoton resonance. Since the energy gap between the two energy levels in the flux ladder system is  $2\tilde{K}$ , resonance occurs when the energy difference between the two energy levels is equal to an integer multiple of the photon energy. Instead, constructive interference fringes occur at the nonresonant points  $2\tilde{K} = (n + \frac{1}{2})\tilde{\omega}_{\parallel}$  in the ladder system. As depicted in Figs. 9(a2)–9(b3), interference patterns become asymmetric about  $\tilde{\omega}_{\perp} = 0$  when the effective atomic interaction is present in the ladder system, and this asymmetry is significantly enhanced as the strength of the effective interaction increases. When  $\tilde{K}/\tilde{\omega}_{\parallel} \rightarrow 0$ , resonance peaks shift with the offset  $|\tilde{U} - \tilde{V}|$ . Comparing Figs. 9(a2) and 9(b2), we can see that the resonance peak of the interference pattern shifts to the right with the attraction effective interaction, and it shifts to the left with the repulsion effective interaction. Therefore, the type and intensity of the interaction in the ladder system can

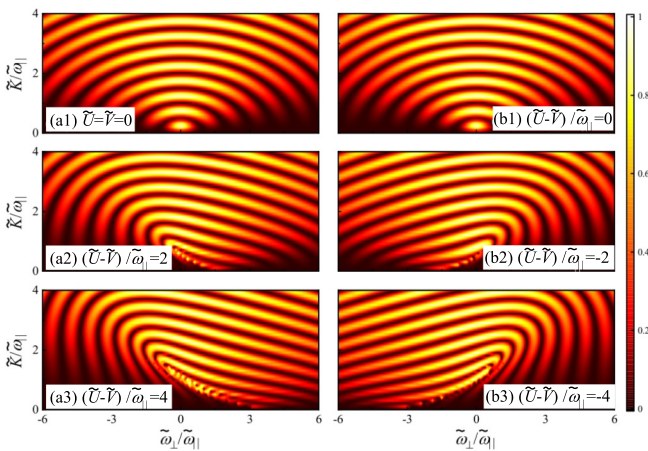


FIG. 9. In the weak driving limit, LZSM interference patterns on the  $(\tilde{K}/\tilde{\omega}_{\parallel}, \tilde{\omega}_{\perp}/\tilde{\omega}_{\parallel})$  plane with different effective interactions. The colorbar represents the population probability  $|a_L|^2$  for the left leg momentum state. The other parameters are  $t_0 = 0$ ,  $t = 2\pi/\tilde{\omega}_{\parallel}$  and  $\phi = 0.002\pi$ .



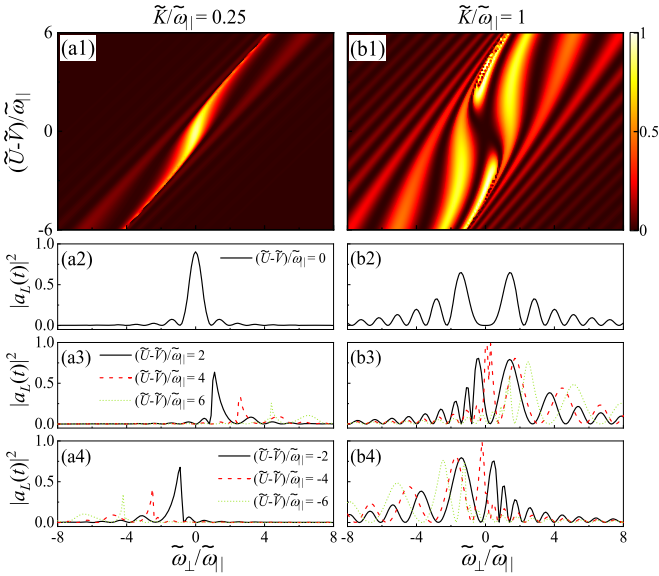


FIG. 10. In the weak driving limit, LZSM interference patterns on the  $((\tilde{U} - \tilde{V})/\tilde{\omega}_{\parallel}, \tilde{\omega}_{\perp}/\tilde{\omega}_{\parallel})$  plane with (a1)  $\tilde{K}/\tilde{\omega}_{\parallel} = 0.25$  and (b1)  $\tilde{K}/\tilde{\omega}_{\parallel} = 1$ . The colorbar represents the population probability  $|a_L|^2$  for the left leg momentum state. (a2–a4) Wave packets of the population probability of the left leg momentum state correspond to (a1) at different effective interactions. (b2–b4) Wave packets of the population probability of the left leg momentum state correspond to (b1) at different effective interactions. The other parameters are  $t_0 = 0$ ,  $t = 2\pi/\tilde{\omega}_{\parallel}$ , and  $\phi = 0.002\pi$ .

be accurately measured from the interference pattern under the weak driving limit.

To further discuss the effect of interaction strength on the asymmetry of the interference pattern, we present the interference pattern on the  $((\tilde{U} - \tilde{V})/\tilde{\omega}_{\parallel}, \tilde{\omega}_{\perp}/\tilde{\omega}_{\parallel})$  plane in Fig. 10. When  $\tilde{K}/\tilde{\omega}_{\parallel} = 0.25$ , which satisfies the constructive interference condition at  $\tilde{\omega}_{\perp} = 0$ , the center of the interference pattern is a bright fringe [see Figs. 10(a1) and 10(a2)]. As the effective interaction strength increases, the peak of the interference pattern shifts and its value decreases [see Figs. 10(a3) and 10(a4)]. Interestingly, the opposite side of the peak shift will have an obvious self-trapping phenomenon. When  $\tilde{K}/\tilde{\omega}_{\parallel} = 1$ , which satisfies the destructive interference condition at  $\tilde{\omega}_{\perp} = 0$ , the center of the interference pattern is a dark fringe [see Figs. 10(b1) and 10(b2)]. Compared with Fig. 10(a1), the area of interference in the biased ladder system significantly increases for a larger coupling ratio  $\tilde{K}$ , which provides an effective way to accurately measure the coupling ratio by utilizing the width of the interference pattern.

In order to investigate the macroscopic self-trapping phenomenon in the biased flux ladder system, we plot the interference pattern on the plane of the interaction and the coupling ratio. As shown in Fig. 11(a), when  $\tilde{K}/\tilde{\omega}_{\parallel} \rightarrow 0$  and the energy bias between the two legs is zero, the interference peak is located at the effective interaction strength  $(\tilde{U} - \tilde{V})/\tilde{\omega}_{\parallel} = 0$ . Moreover, there is an obvious critical line  $|\tilde{U} - \tilde{V}|/\tilde{K} = 4$  in the figure. The amplitude of the interference above the critical line is between 0 and 1, while the amplitude of the interference decreases sharply below the critical line, i.e., the ladder system exhibits the macroscopic

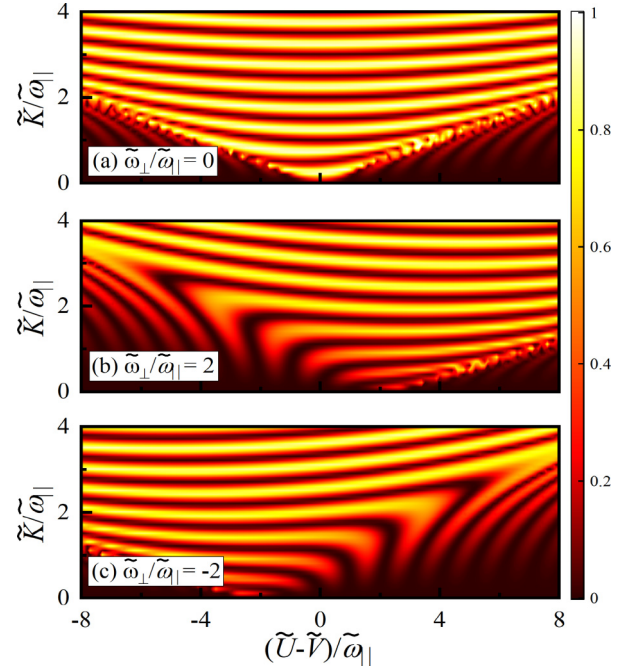


FIG. 11. In the weak driving limit, LZSM interference patterns on the  $((\tilde{U} - \tilde{V})/\tilde{\omega}_{\parallel}, \tilde{K}/\tilde{\omega}_{\parallel})$  plane with different energy biases. The colorbar represents the population probability  $|a_L|^2$  for the left leg momentum state. The other parameters are  $t_0 = 0$ ,  $t = 2\pi/\tilde{\omega}_{\parallel}$ , and  $\phi = 0.002\pi$ .

self-trapping, which is consistent with the discussion in Sec. IV B. As shown in Fig. 11(b), when the energy bias between the two legs is positive, the resonance peak shifts towards the right. A distinct critical line appears on the right side of the interference pattern, maintaining the same slope as before but translating to the right by a distance equal to the energy bias. Interestingly, this macroscopic self-trapping critical line no longer exists on the left side of the interference pattern, and the amplitude of the interference gradually decreases with decreasing  $\tilde{K}$ . Therefore, the energy bias between the two legs can be accurately measured by the translation distance of the resonance peak. In Fig. 11(c), when the energy bias between the two legs is negative, the resonance peak moves towards the left, and the region where the macroscopic self-trapping occurs is obviously on the left side of the interference pattern. It is evident that the self-trapping induced by the interaction primarily modifies the shape of the interference pattern in the unbiased ladder system. The energy bias between the two legs mainly affects the asymmetry of the interference pattern when different interaction terms are dominant.

#### D. Strong driving limit

In the strong driving limit, the amplitude of the driving field is much larger than the driving force and the energy gap between the two adiabatic states is  $2\tilde{K}$ . Therefore, the condition  $4 \sin \frac{\phi}{2} \tilde{\omega}_{\parallel} \gg \tilde{K}^2$  is always met and Eq. (7) can be simplified as

$$i\dot{a}'_L(t) = -\tilde{K} \sum_{n=-\infty}^{\infty} J_n \left( \frac{4 \sin \frac{\phi}{2}}{\tilde{\omega}_{\parallel}} \right) (-i)^n e^{i[\tilde{\omega}_{\perp} - (\tilde{U} - \tilde{V}) - n\tilde{\omega}_{\parallel}]} a'_R(t),$$

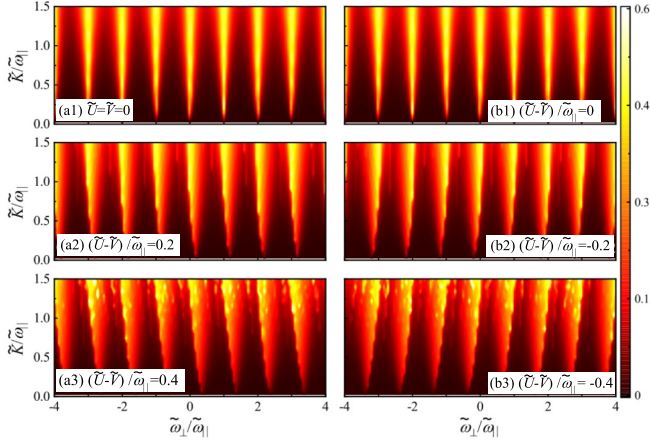


FIG. 12. In the strong driving limit, LZSM interference patterns on the  $(\tilde{\omega}_\perp/\tilde{\omega}_\parallel, \tilde{K}/\tilde{\omega}_\parallel)$  plane with different effective interactions. The colorbar represents the time-averaged population probability  $|\bar{a}_L|^2$  for the left leg momentum state. The other parameters are  $t_0 = 0$ ,  $t = 50\pi/\tilde{\omega}_\parallel$ , and  $\phi = \pi$ .

$$i\dot{a}'_R(t) = -\tilde{K} \sum_{n=-\infty}^{\infty} J_n \left( \frac{4 \sin \frac{\phi}{2}}{\tilde{\omega}_\parallel} \right) (-i)^n e^{-i[\tilde{\omega}_\perp - (\tilde{U} - \tilde{V}) - n\tilde{\omega}_\parallel]t} a'_L(t). \quad (19)$$

At the limit of  $\tilde{K}/\tilde{\omega}_\parallel \rightarrow 0$ , the resonance condition is  $\tilde{\omega}_\perp - (\tilde{U} - \tilde{V}) - n\tilde{\omega}_\parallel = 0$ . We use the time-averaged occupation probability of the left leg momentum state

$$|\bar{a}_L|^2 = \frac{1}{t - t_0} \int_{t_0}^t |a_L(t')|^2 dt' \quad (20)$$

to describe the LZSM interferometry of the biased ladder system, where  $t_0 = 0$ ,  $t = 50\pi/\tilde{\omega}_\parallel$ . As shown in Figs. 12(a1) and 12(b1), when considering the noninteracting ladder system (or the system with the effective interaction  $|\tilde{U} - \tilde{V}| = 0$ ), we observe multiple interference peaks at  $\tilde{K}/\tilde{\omega}_\parallel \rightarrow 0$ , and the interference peaks are located at  $\tilde{\omega}_\perp = n\tilde{\omega}_\parallel - (\tilde{U} - \tilde{V})$ , where  $n = -4, -3, \dots, 4, 5$ . As the rung-to-leg coupling ratio increases, resonance peaks of the system are gradually broadened. In Figs. 12(a2) and 12(a3), when the effective interaction is repulsive, i.e.,  $\tilde{U} > \tilde{V}$ , the interference peaks of the system are shifted to the right by a distance of  $|\tilde{U} - \tilde{V}|$ . Additionally, the structure of each interference peak is no longer symmetric with respect to left and right, which is mainly concentrated on the left side. With further increase of the on-site interaction, the asymmetry of the interference pattern is significantly enhanced. When the effective interaction is attractive, i.e.,  $\tilde{U} < \tilde{V}$ , the interference patterns are antisymmetric compared to the previous case, which is mainly concentrated on the right side [see Figs. 12(b2) and 12(b3)]. The interference peaks in LZSM interference at the strong driving limit are very sharp, making it an ideal playground for precise measurements of weak atomic interactions.

To further show the influence of the interaction on the symmetry of the interference pattern of the system, we present the interference pattern on the plane of the effective interaction and the energy bias in Fig. 13. When  $t = 50\pi/\tilde{\omega}_\parallel$ , the first line

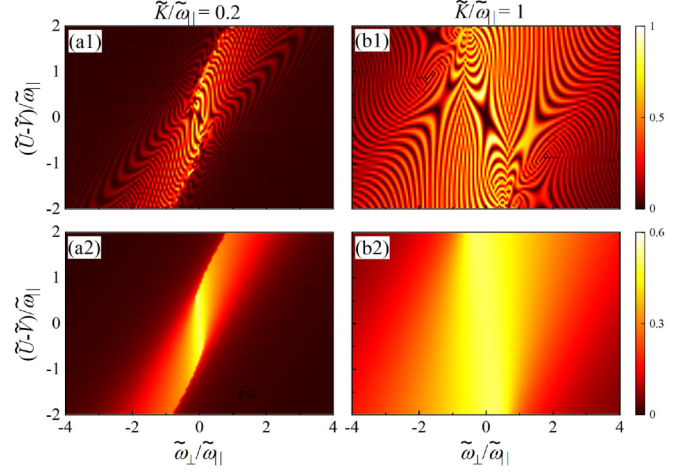


FIG. 13. In the strong driving limit, LZSM interference patterns on the  $(\tilde{K}/\tilde{\omega}_\parallel, \tilde{\omega}_\perp/\tilde{\omega}_\parallel)$  plane with different rung-to-leg coupling ratios. The colorbar of (a1) and (b1) represents the population probability  $|a_L|^2$  for the left leg momentum state. The colorbar of (a2) and (b2) represents the time-averaged population probability  $|\bar{a}_L|^2$  for the left leg momentum state. The other parameters are  $t_0 = 0$ ,  $t = 50\pi/\tilde{\omega}_\parallel$ , and  $\phi = \pi$ .

and the second line of Fig. 13 show the population probability  $|a_L(t)|^2$  and the time-averaged population probability  $|\bar{a}_L|^2$  for the left leg momentum state, respectively. In Figs. 13(a1) and 13(b1), the interference pattern is a tilted ribbonlike structure consisting of helical interference fringes. The range of the interference pattern expands with the increasing of rung-to-leg coupling ratio, and the strength of the interference is inversely proportional to the magnitude of the energy bias. The corresponding interference patterns of the time-averaged population probability are shown in Figs. 13(a2) and 13(b2); the helical interference fringes disappear, which indicates that the helical interference fringes evenly appear on the plane during the interference process. It is worth noting that the intensity of the interference is still maintained, suggesting that the intensity of the interference pattern is mainly determined by the intensity of the energy bias.

## V. SUMMARY AND DISCUSSION

In conclusion, we discuss the LZSM tunneling dynamics and its interference phenomenon of the extended Bose-Hubbard flux ladder. Considering the on-site atomic interaction and long-range interaction in the rung direction, the nonlinear dispersion relation of the ladder system is solved by means of the mean-field theory. The nonlinear energy band characteristics and the unique chirality of the flux ladder system are reflected in the nonlinear Landau-Zener tunneling process. The tunneling probability depends on the strength of the gravitational field, effective interaction, rung-to-leg coupling ratio, and magnetic field. In addition, the periodicity of the energy band structure of the flux ladder system provides an ideal playground to realize the nonlinear LZSM interference without Floquet engineering. Remarkably, we find that the noise of the interference occurs when the energy band of the biased ladder system has the loop structure,

which reveals an effective link between the nonlinear loop structure and LZSM interferometry. Moreover, the resonance conditions for the occurrence of nonlinear LZSM interference in the extended Bose-Hubbard flux ladder are analytically given in four extreme cases, and the corresponding interference patterns are shown by the numerical simulations, which verifies the theoretical predications. The interference pattern strongly depends on the magnetic flux, rung-to-leg coupling ratio, effective interaction, and energy bias. Therefore, the unique properties of the interference pattern can be used to accurately measure these parameters of the flux ladder system in experiments. This paper will further extend the dynamics research of the magnetic ladder system to the extended Bose-Hubbard flux ladder system with complex interactions, filling the research gap of nonlinear dynamic effects in this system and also providing an efficient way for precise measurements.

Note that the LZSM tunneling dynamics and interference phenomenon considered in our paper are at zero temperature. However, real experiment is always at finite temperature. Because of thermal fluctuations, the dynamical relaxation and phase decoherence will occur as temperature  $\tilde{T}$  ( $\tilde{T} = T/J$ ) increases [90–92]. For a regime with large driving force  $\tilde{\omega}_{\parallel} \gg 4\tilde{K}^2$ , it has been found that a thermal heat bath has

no influence on the Landau-Zener transitions, while for small driving force  $\tilde{\omega}_{\parallel}$  the LZ probability decreases with increasing temperatures [90,91]. However, it is shown that [90], when  $\tilde{T} \ll 4\tilde{K}$ , Landau-Zener transitions are in good agreement with the case in zero temperatures. Therefore, the nonlinear dynamical phenomena discussed in our paper can be clearly observed under the above-mentioned temperature conditions, which are achievable in current experiments [38].

#### ACKNOWLEDGMENTS

This work is supported by the National Natural Science Foundation of China under Grants No. 12164042, No. 12264045, No. 11764039, and No. 11847304; by China Postdoctoral Science Foundation under Grant No. 2023M732260; by Natural Science Foundation of Gansu province under Grants No. 22JR5RA174, No. 20JR5RA526, and No. 17JR5RA076; by Scientific Research Project of Gansu Higher Education under Grant No. 2016A-005; by Innovation Capability Enhancement Project of Gansu Higher Education under Grants No. 2022A-011, No. 2020A-146, and No. 2019A-014; and by Creation of Science and Technology of Northwest Normal University under Grants No. NWNLU-LKQN2022-05 and No. NWNLU-LKQN-18-33.

- 
- [1] L. D. Landau, *Phys. Z. Sowjetunion* **2**, 46 (1932).
  - [2] C. Zener, *Proc. R. Soc. A* **137**, 696 (1932).
  - [3] V. S. Shchesnovich, S. B. Cavalcanti, J. M. Hickmann, and Y. S. Kivshar, *Phys. Rev. E* **74**, 056602 (2006).
  - [4] V. Loladze and R. Khomeriki, *Phys. Rev. E* **95**, 042204 (2017).
  - [5] M. S. Child, *Molecular Collision Theory* (Courier, New York, 1996).
  - [6] K. Saito and Y. Kayanuma, *Phys. Rev. B* **70**, 201304(R) (2004).
  - [7] W. Wernsdorfer, M. Murugesu, and G. Christou, *Phys. Rev. Lett.* **96**, 057208 (2006).
  - [8] Z. G. Chen, W. Tang, R. Y. Zhang, Z. Chen, and G. Ma, *Phys. Rev. Lett.* **126**, 054301 (2021).
  - [9] A. Xie, S. Zhou, K. Xi, L. Ding, Y. Pan, Y. Ke, H. Wang, S. Zhuang, and Q. Cheng, *Phys. Rev. B* **106**, 174301 (2022).
  - [10] J. Ankerhold and H. Grabert, *Phys. Rev. Lett.* **91**, 016803 (2003).
  - [11] G. Ithier, E. Collin, P. Joyez, D. Vion, D. Estève, J. Ankerhold, and H. Grabert, *Phys. Rev. Lett.* **94**, 057004 (2005).
  - [12] S. N. Shevchenko, S. Ashhab, and F. Nori, *Phys. Rep.* **492**, 1 (2010).
  - [13] P. Plötz and S. Wimberger, *Eur. Phys. J. D* **65**, 199 (2011).
  - [14] Q. Xie, *Phys. Rev. A* **97**, 022113 (2018).
  - [15] F. Forster, G. Petersen, S. Manus, P. Hänggi, D. Schuh, W. Wegscheider, S. Kohler, and S. Ludwig, *Phys. Rev. Lett.* **112**, 116803 (2014).
  - [16] D. V. Khomitsky and S. A. Studenikin, *Phys. Rev. B* **106**, 195414 (2022).
  - [17] L. Y. Gorelik, N. I. Lundin, V. S. Shumeiko, R. I. Shekhter, and M. Jonson, *Phys. Rev. Lett.* **81**, 2538 (1998).
  - [18] A. L. Gramajo, D. Domínguez, and M. J. Sánchez, *Phys. Rev. B* **100**, 075410 (2019).
  - [19] C. Calero, E. M. Chudnovsky, and D. A. Garanin, *Phys. Rev. B* **72**, 024409 (2005).
  - [20] M. J. Seitner, H. Ribeiro, J. Kölbl, T. Faust, and E. M. Weig, *New J. Phys.* **19**, 033011 (2017).
  - [21] M. Bonifacio, D. Domínguez, and M. J. Sánchez, *Phys. Rev. B* **101**, 245415 (2020).
  - [22] P. Földi, M. Benedict, J. M. Pereira, Jr., and F. M. Peeters, *Phys. Rev. B* **75**, 104430 (2007).
  - [23] B. Wu and Q. Niu, *Phys. Rev. A* **61**, 023402 (2000).
  - [24] J. Liu, L. B. Fu, B. Y. Ou, S. G. Chen, D. I. Choi, B. Wu, and Q. Niu, *Phys. Rev. A* **66**, 023404 (2002).
  - [25] G. F. Wang, D. F. Ye, L. B. Fu, X. Z. Chen, and J. Liu, *Phys. Rev. A* **74**, 033414 (2006).
  - [26] F. Trimborn, D. Witthaut, V. Kegel, and H. J. Korsch, *New J. Phys.* **12**, 053010 (2010).
  - [27] Q. Zhang, P. Hänggi, and J. Gong, *New J. Phys.* **10**, 073008 (2008).
  - [28] Y. Zhang, Z. Gui, and Y. Chen, *Phys. Rev. A* **99**, 023616 (2019).
  - [29] G. Watanabe, S. Yoon, and F. Dalfovo, *Phys. Rev. Lett.* **107**, 270404 (2011).
  - [30] Y. Zhang, Z. Chen, B. Wu, T. Busch, and V. V. Konotop, *Phys. Rev. Lett.* **127**, 034101 (2021).
  - [31] S. C. Li, L. B. Fu, and J. Liu, *Phys. Rev. A* **98**, 013601 (2018).
  - [32] X. Shen, F. Wang, Z. Li, and Z. Wu, *Phys. Rev. A* **100**, 062514 (2019).
  - [33] B. Longstaff and E.-M. Graefe, *Phys. Rev. A* **100**, 052119 (2019).
  - [34] X. Wang, H. D. Liu, and L. B. Fu, *New J. Phys.* **25**, 043032 (2023).
  - [35] W. Y. Wang, B. Sun, and J. Liu, *Phys. Rev. A* **106**, 063708 (2022).



- [36] P. Donohue and T. Giamarchi, *Phys. Rev. B* **63**, 180508(R) (2001).
- [37] E. Orignac and T. Giamarchi, *Phys. Rev. B* **64**, 144515 (2001).
- [38] M. Atala, M. Aidelsburger, M. Lohse, J. T. Barreiro, B. Paredes, and I. Bloch, *Nat. Phys.* **10**, 588 (2014).
- [39] K. Çeven, M. Ö. Oktel, and A. Keleş, *Phys. Rev. A* **106**, 063320 (2022).
- [40] Y. He, R. Mao, H. Cai, J. X. Zhang, Y. Li, L. Yuan, S. Y. Zhu, and D. W. Wang, *Phys. Rev. Lett.* **126**, 103601 (2021).
- [41] X. Yu and S. Flach, *Phys. Rev. E* **90**, 032910 (2014).
- [42] B. Stuhl, H. I. Lu, L. Ayccock, D. Genkina, and I. Spielman, *Science* **349**, 1514 (2015).
- [43] M. Mancini, G. Pagano, G. Cappellini, L. Livi, M. Rider, J. Catani, C. Sias, P. Zoller, M. Inguscio, M. Dalmonte *et al.*, *Science* **349**, 1510 (2015).
- [44] M. Buser, U. Schollwöck, and F. Grusdt, *Phys. Rev. A* **105**, 033303 (2022).
- [45] A. Petrescu and K. Le Hur, *Phys. Rev. Lett.* **111**, 150601 (2013).
- [46] M. Piraud, F. Heidrich-Meisner, I. P. McCulloch, S. Greschner, T. Vekua, and U. Schollwöck, *Phys. Rev. B* **91**, 140406(R) (2015).
- [47] E. Orignac, R. Citro, M. Di Dio, S. De Palo, and M.-L. Chiofalo, *New J. Phys.* **18**, 055017 (2016).
- [48] A. Keleş and M. Ö. Oktel, *Phys. Rev. A* **91**, 013629 (2015).
- [49] X. Qiao, X. B. Zhang, Y. Jian, A. X. Zhang, Z. F. Yu, and J. K. Xue, *Phys. Rev. A* **104**, 053323 (2021).
- [50] A. Dhar, M. Maji, T. Mishra, R. V. Pai, S. Mukerjee, and A. Paramekanti, *Phys. Rev. A* **85**, 041602(R) (2012).
- [51] S. Greschner and T. Vekua, *Phys. Rev. Lett.* **119**, 073401 (2017).
- [52] R. Wei and E. J. Mueller, *Phys. Rev. A* **89**, 063617 (2014).
- [53] M. Buser, C. Hubig, U. Schollwöck, L. Tarruell, and F. Heidrich-Meisner, *Phys. Rev. A* **102**, 053314 (2020).
- [54] S. Sajid and A. Chakrabarti, *Phys. Rev. B* **102**, 134401 (2020).
- [55] G. Sun, *Phys. Rev. A* **93**, 023608 (2016).
- [56] D. Hügél and B. Paredes, *Phys. Rev. A* **89**, 023619 (2014).
- [57] Y. Zheng, S. Feng, and S. J. Yang, *Phys. Rev. A* **96**, 063613 (2017).
- [58] X. Qiao, X. B. Zhang, A. X. Zhang, Z. F. Yu, and J. K. Xue, *Phys. Lett. A* **383**, 3095 (2019).
- [59] S. Liang, Z. C. Li, W. Zhang, L. Zhou, and Z. Lan, *Phys. Rev. A* **102**, 033332 (2020).
- [60] M. E. Tai, A. Lukin, M. Rispoli, R. Schittko, T. Menke, D. Borgnia, P. M. Preiss, F. Grusdt, A. M. Kaufman, and M. Greiner, *Nature (London)* **546**, 519 (2017).
- [61] A. Celi, P. Massignan, J. Ruseckas, N. Goldman, I. B. Spielman, G. Juzeliūnas, and M. Lewenstein, *Phys. Rev. Lett.* **112**, 043001 (2014).
- [62] L. Yuan, Q. Lin, M. Xiao, and S. Fan, *Optica* **5**, 1396 (2018).
- [63] T. Ozawa and H. M. Price, *Nat. Rev. Phys.* **1**, 349 (2019).
- [64] B. Y. Sun, X. W. Luo, M. Gong, G. C. Guo, and Z. W. Zhou, *Phys. Rev. A* **96**, 013857 (2017).
- [65] G. Li, Y. Zheng, A. Dutt, D. Yu, Q. Shan, S. Liu, L. Yuan, S. Fan, and X. Chen, *Sci. Adv.* **7**, eabe4335 (2021).
- [66] L. Taddia, E. Cornfeld, D. Rossini, L. Mazza, E. Sela, and R. Fazio, *Phys. Rev. Lett.* **118**, 230402 (2017).
- [67] G. Li, L. Wang, R. Ye, S. Liu, Y. Zheng, L. Yuan, and X. Chen, *Adv. Photonics* **4**, 036002 (2022).
- [68] A. Dutt, Q. Lin, L. Yuan, M. Minkov, M. Xiao, and S. Fan, *Science* **367**, 59 (2020).
- [69] Y. Li, J. Zhang, Y. Wang, H. Du, J. Wu, W. Liu, F. Mei, J. Ma, L. Xiao, and S. Jia, *Light Sci. Appl.* **11**, 13 (2022).
- [70] H. Cai, J. Liu, J. Wu, Y. He, S. Y. Zhu, J. X. Zhang, and D. W. Wang, *Phys. Rev. Lett.* **122**, 023601 (2019).
- [71] Y. J. Zhao, X. W. Xu, H. Wang, Y. X. Liu, and W. M. Liu, *Phys. Rev. A* **102**, 053722 (2020).
- [72] Y. J. Zhao, N. Tan, D. Yu, B. Liu, and W. M. Liu, *Phys. Rev. Res.* **2**, 033484 (2020).
- [73] A. J. Olson, D. B. Blasing, C. Qu, C.-H. Li, R. J. Niffenegger, C. Zhang, and Y. P. Chen, *Phys. Rev. A* **95**, 043623 (2017).
- [74] B. P. Anderson and M. A. Kasevich, *Science* **282**, 1686 (1998).
- [75] G. Roati, E. De Mirandes, F. Ferlaino, H. Ott, G. Modugno, and M. Inguscio, *Phys. Rev. Lett.* **92**, 230402 (2004).
- [76] W. M. Liu, W. B. Fan, W. M. Zheng, J. Q. Liang, and S. T. Chui, *Phys. Rev. Lett.* **88**, 170408 (2002).
- [77] Q. Niu, X.-G. Zhao, G. A. Georgakis, and M. G. Raizen, *Phys. Rev. Lett.* **76**, 4504 (1996).
- [78] C. F. Bharucha, K. W. Madison, P. R. Morrow, S. R. Wilkinson, B. Sundaram, and M. G. Raizen, *Phys. Rev. A* **55**, R857 (1997).
- [79] F. S. Cataliotti, S. Burger, C. Fort, P. Maddaloni, F. Minardi, A. Trombettoni, A. Smerzi, and M. Inguscio, *Science* **293**, 843 (2001).
- [80] C. Chin, R. Grimm, P. Julienne, and E. Tiesinga, *Rev. Mod. Phys.* **82**, 1225 (2010).
- [81] L.-C. Ha, C.-L. Hung, X. Zhang, U. Eismann, S.-K. Tung, and C. Chin, *Phys. Rev. Lett.* **110**, 145302 (2013).
- [82] T. Salger, C. Geckeler, S. Kling, and M. Weitz, *Phys. Rev. Lett.* **99**, 190405 (2007).
- [83] P. Cladé, S. Guellati-Khélifa, C. Schwob, F. Nez, L. Julien, and F. Biraben, *Europhys. Lett.* **71**, 730 (2005).
- [84] N. Poli, F.-Y. Wang, M. G. Tarallo, A. Alberti, M. Prevedelli, and G. M. Tino, *Phys. Rev. Lett.* **106**, 038501 (2011).
- [85] G. Ferrari, N. Poli, F. Sorrentino, and G. M. Tino, *Phys. Rev. Lett.* **97**, 060402 (2006).
- [86] B. M. Caradoc-Davies, Ph.D. thesis, University of Otago, 2000.
- [87] L. B. Fu and J. Liu, *Phys. Rev. A* **74**, 063614 (2006).
- [88] C. Ottaviani, V. Ahufinger, R. Corbalán, and J. Mompert, *Phys. Rev. A* **81**, 043621 (2010).
- [89] Y. Zheng, S. Feng, and S. J. Yang, *Phys. Rev. A* **97**, 043627 (2018).
- [90] P. Nalbach and M. Thorwart, *Phys. Rev. Lett.* **103**, 220401 (2009).
- [91] L. Arceci, S. Barbarino, R. Fazio, and G. E. Santoro, *Phys. Rev. B* **96**, 054301 (2017).
- [92] W.-X. Liu, T. Wang, X.-F. Zhang, and W.-D. Li, *Phys. Rev. A* **104**, 053318 (2021).